Supplement of The Cryosphere, 15, 2273–2293, 2021
https://doi.org/10.5194/tc-15-2273-2021-supplement

The Cryosphere
Open Access

Supplement of

The surface energy balance in a cold and arid permafrost environment, Ladakh, Himalayas, India

John Mohd Wani et al.

Correspondence to: John Mohd Wani (johnn.nith@gmail.com)

Table S1: Comparison between observed and ESOLIP estimated precipitation from 1 September 2015 to 31 August 2017 at South-Pullu (4727 m a.s.l.).

Year	Annual Sum	
	Field Obs. (mm w.e.)	ESOLIP Est. (mm w.e.)
2015-16	120.3	92.2
2016-17	190.6	292.5
Total	310.9	384.7

Table S2: Comparison of estimated mean monthly surface energy balance components (W m^{-2}) for low (2015-16) and high (2016-17) snow years at South-Pullu (4727 m a.s.l.), in the upper Ganglass catchment, Leh.

Month	**R_n** [$W\ m^{-2}$]		**LE** [$W\ m^{-2}$]		**H** [$W\ m^{-2}$]		**G** [$W\ m^{-2}$]		**F_{surf}** [$W\ m^{-2}$]	
	2015-16	**2016-17**	**2015-16**	**2016-17**	**2015-16**	**2016-17**	**2015-16**	**2016-17**	**2015-16**	**2016-17**
Sep	55.7	50.7	-6.2	-5.1	-47.1	-40.9	-1.9	-4.7	-2.4	-4.7
Oct	20.4	29.5	-1.2	-0.5	-22.9	-33.2	3.8	4.2	3.8	4.2
Nov	1.5	5.3	0.3	0.5	-15.3	-18.2	13.5	12.5	13.5	12.5
Dec	-25.8	-11.8	2.5	0.5	-1.3	-4.7	24.6	16.0	24.6	16.0
Jan	-37.9	-20.2	-3.4	-6.8	24.1	10.9	16.5	16.1	17.2	16.1
Feb	-34.0	-22.7	-7.6	-3.8	32.9	22.1	8.4	4.5	8.7	4.4
Mar	-2.2	-12.6	-17.8	-7.3	17.6	16.9	4.7	3.8	2.4	3.0
Apr	40.2	0.7	-17.4	-12.8	-11.7	14.5	-2.3	0.4	-11.1	-2.4
May	92.7	80.2	-29.9	-26.4	-42.9	-2.0	-19.9	-11.2	-19.9	-51.8
Jun	81.0	88.2	-7.9	-39.7	-52.4	-29.8	-20.8	-17.9	-20.8	-18.6
Jul	78.9	99.6	-6.9	-48.5	-54.7	-30.7	-17.4	-20.4	-17.4	-20.4
Aug	72.4	75.8	-8.1	-14.5	-53.3	-49.2	-10.8	-12.1	-11.0	-12.1
Annual Av.	**28.6**	**30.2**	**-8.6**	**-13.7**	**-18.9**	**-12.0**	**-0.1**	**-0.7**	**-1.0**	**-4.5**

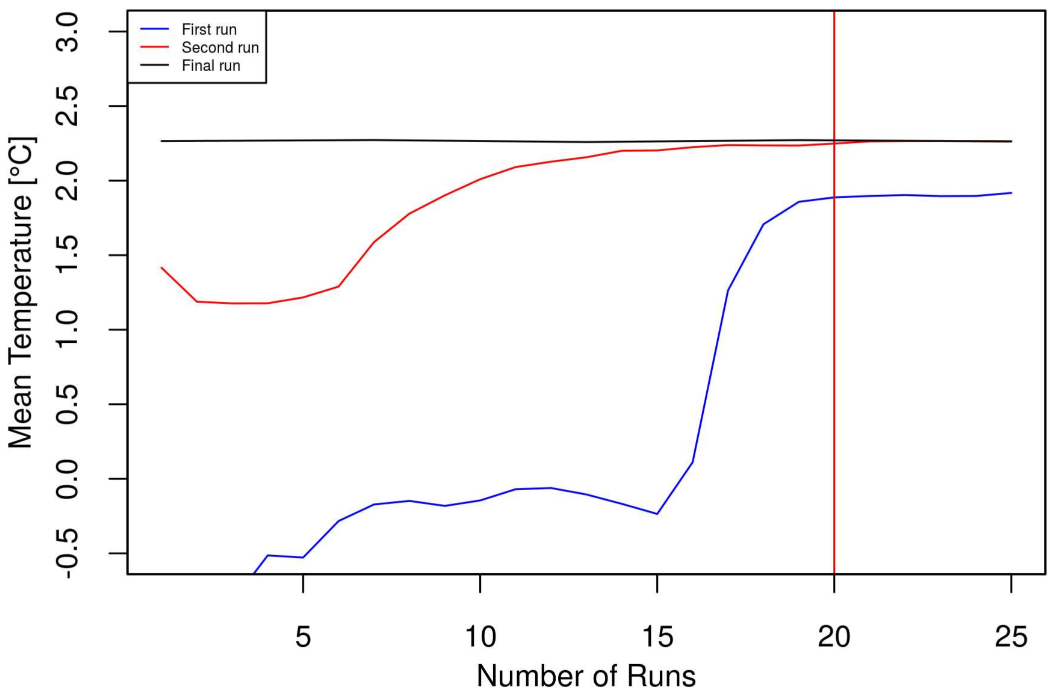

Figure S1: Temperature variations of the model MAGST at 10 cm depth for an increasing number of simulations. Convergence is reached at approximately 25 simulations

Performance statistics for evaluation of outgoing longwave radiation

For the evaluation of outgoing longwave radiation, we prefer the statistics mean bias difference (MBD) and the root mean square difference (RMSD) (Badescu et al., 2012; Gubler et al., 2012; Gueymard, 2012). These statistics indicate model prediction accuracy (Stow et al., 2003).

The **MBD** (Eq. S1) is a simple and familiar measure that neglects the magnitude of the errors (i.e. positive errors can compensate for negative ones) (Gubler et al., 2012):

$$\boldsymbol{MBD} = \frac{\mathbf{1}}{\overline{\overline{\boldsymbol{y}^*}}} \frac{\sum_{t=1}^{n}(\boldsymbol{y_t} - \boldsymbol{y_t^*})}{\boldsymbol{n}} \qquad \textbf{(S1)}$$

Here, y_t is the modelled output variable, and y_t^* is the corresponding measured variable. The MBD ranges from -∞ to ∞. The perfect model is the one with an MBD value equal to 0.

The **RMSD** (Eq. S2) is calculated as (Gubler et al., 2012):

$$\boldsymbol{RMSD} = \frac{\mathbf{1}}{\overline{\overline{\boldsymbol{y}^*}}} \sqrt{\frac{\mathbf{1}}{\boldsymbol{n}} \sum_{t=1}^{n} (\boldsymbol{y_t} - \boldsymbol{y_t^*})^2} \qquad \textbf{(S2)}$$

The RMSD takes into account the average magnitude of the errors and puts weight on larger errors, but neglects the direction of the errors (Gubler et al., 2012). The RMSD ranges from 0 to

∞. The perfect model is the one with an RMSD value equal to 0. The formulae (Eq. S1 and S2) used for estimation of MBD and RMSD respectively provide dimensionless quantities since their right-hand side has been divided by the mean of the measured variable (Badescu et al., 2012). Hence, they are expressed in per cent throughout the manuscript for clarity.

Coefficient of determination (**R^2**, Eq. S3): is defined as the squared value of the coefficient of correlation which indicates the amount of variation in the modelled variable predictable from the measured variable:

$$R^2 = \left(\frac{\sum_{t=1}^{n} (y_t - \overline{y})\,(y_t^* - \overline{y^*})}{\sqrt{\sum_{t=1}^{n} (y_t - \overline{y})^2 (y_t^* - \overline{y^*})^2}} \right)^2 \quad \textbf{(S3)}$$

Where $\overline{y^*}$ is the mean of the measured variable.

Performance statistics for evaluation of snow depth and near-surface ground temperature

For the evaluation of near-surface ground temperature and snow depth apart from the coefficient of determination (R^2), different statistical measures have been used such as mean bias (MB), and root mean square error (RMSE).

Mean Bias (MB): The MB (Eq. S4) provides a good indication of the mean over or underestimate of predictions (Carslaw and Ropkins, 2012). MB is in the same units as the variables being considered.

$$MB = \frac{1}{n} \sum_{i=1}^{n} (y_t - y_t^*) \quad \textbf{(S4)}$$

The optimal value of MB is equal to zero. The positive and negative MB values indicate model over-estimation and under-estimation bias, respectively.

Root Mean Square Error (RMSE): The RMSE (Moriasi et al., 2007) is a commonly used statistic that provides a good overall measure of how close modelled values are to predicted values and is given below (Eq. S5):

$$RMSE = \sqrt{\frac{1}{n} \sum_{t=1}^{n} (y_t - y_t^*)^2} \quad \textbf{(S5)}$$

Nash-Sutcliffe efficiency (NSE): The Nash-Sutcliffe efficiency (NSE) (Eq. S6) is a normalized statistic that determines the relative magnitude of the residual variance (“noise”) compared to the measured data variance (“information”) (Moriasi et al., 2007; Nash and Sutcliffe, 1970).

$$\boldsymbol{NSE = 1 - \left[\frac{\sum_{t=1}^{n}(y_t - y_t^*)^2}{\sum_{t=1}^{n}(y_t - \overline{y^*})^2}\right]} \quad \textbf{(S6)}$$

NSE indicates how well the plot of observed versus simulated data fits the 1:1 line.

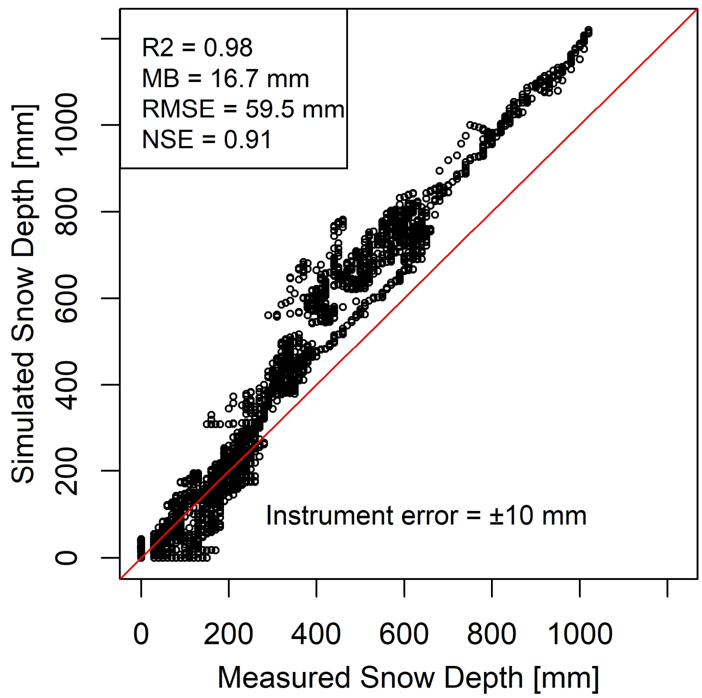

Figure S2: Comparison of hourly observed and GEOtop simulated snow depth at 4727 m a.s.l. in the upper Ganglass catchment, Leh from September 2015 to August 2017. The solid red line is the 1:1 line.

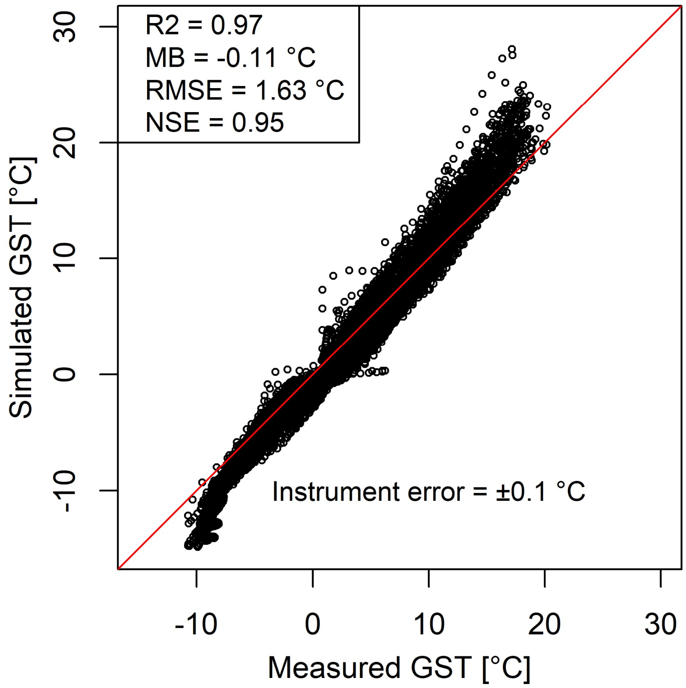

Figure S3: Comparison of hourly observed and GEOtop simulated near-surface ground temperature at 4727 m a.s.l. in the upper Ganglass catchment, Leh from September 2016 to August 2017. The solid red line is the 1:1 line.

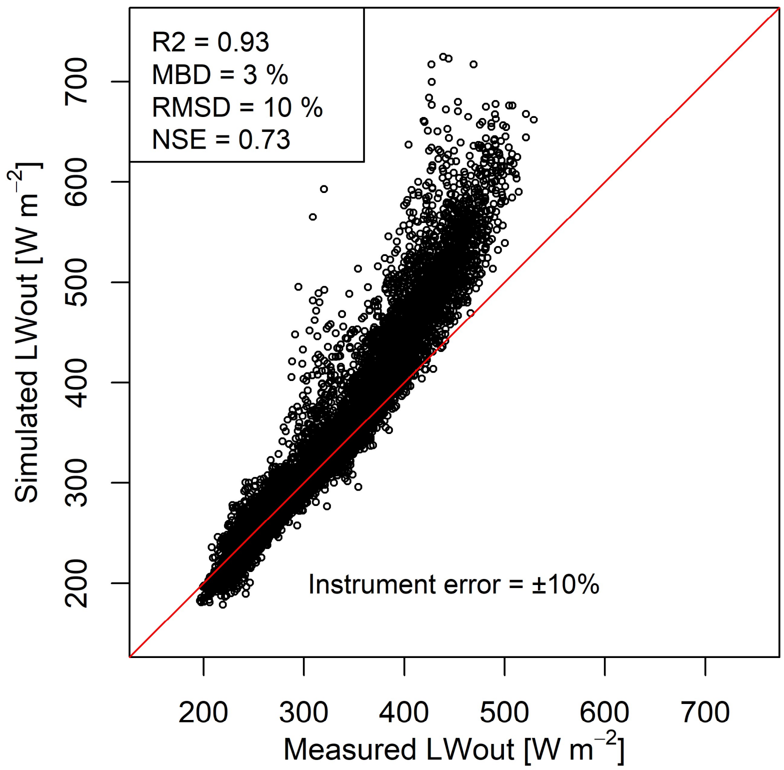

Figure S4: Comparison of hourly observed and GEOtop simulated outgoing longwave radiation at 4727 m a.s.l. in the upper Ganglass catchment, Leh from September 2016 to August 2017. The solid red line is the 1:1 line.

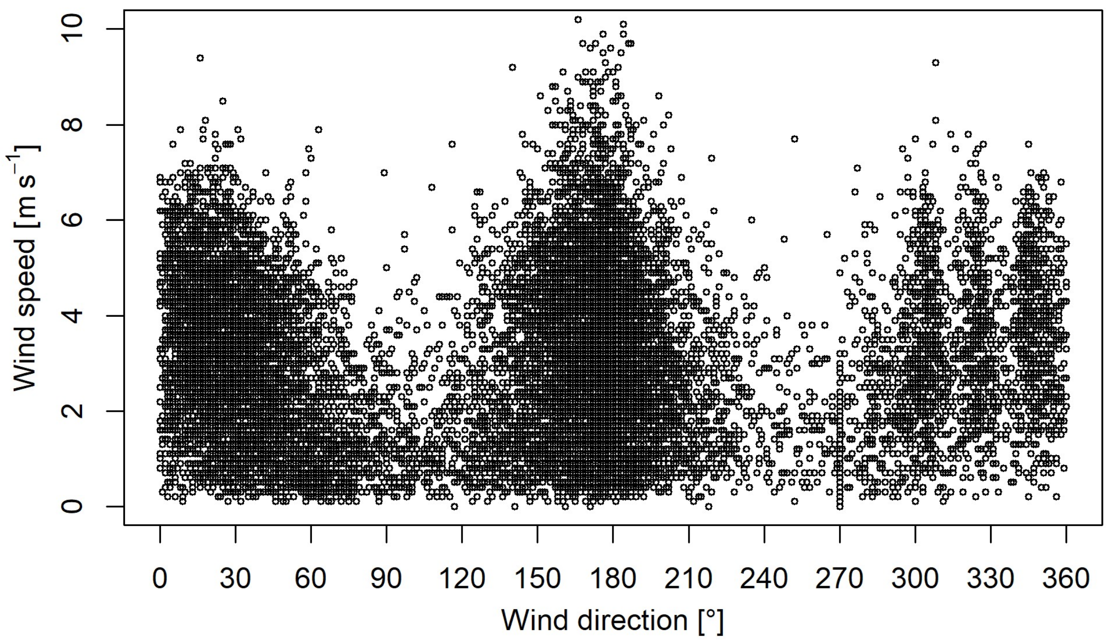

Figure S5: Comparison of hourly observed wind speed (m s^{-1}) as a function of hourly wind direction (°) at 4727 m a.s.l. in the upper Ganglass catchment, Leh from September 2015 to August 2017.

Seasonal diurnal variability of SEB components

The seasonal response of diurnal variation of modelled SEB components (R_n, LE, H and G) for both years are shown in Figures *S6* and *S7*, respectively. The seasons chosen were pre-winter (Sep to Dec), winter (Jan to Apr), post-winter (May-Jun), and summer (Jul to Aug).

In the 2015–16 year (Figure *S6*), the amplitude of R_n and the G during pre-winter, post-winter and summer season were the largest and smallest in winter. The G peaks earlier than those of the LE and H during the pre-winter, post-winter and summer season. The LE and H show strong seasonal characteristics such as (a) during the pre-winter season, the magnitude of diurnal variation of H was greater than LE depicting lesser soil moisture content because of freezing conditions at that time, (b) during the winter season, the amplitude of LE was slightly greater (sublimation process) than H, (c) during the post-winter, the amplitude of H was greater than LE and, (d) during the summer season, again the amplitude of H was greater than LE, which is similar to that of the pattern seen during the pre-winter season. In the 2015-16 year, the amplitude of LE in comparison to H was smaller in summer season due to the lesser precipitation and lesser moisture availability. The R_n and G increased rapidly after the sunrise and changed the direction during pre-winter, post-winter and summer seasons. After sunset, the R_n and G again change sign rapidly, but the LE and H gradually decreased to lower values. The LE and H in the morning increased 1 to 2 hours after the R_n during pre-, post-winter and summer season.

In the 2016–17 year (Figure *S7*), the pre-winter, winter and summer were the same as that of the 2015–16 year except for the amplitude of LE in was larger in summer season due to the more precipitation and more moisture availability. However, during the winter and post-winter season of the 2016–17 year, the main difference in diurnal changes was found because of the extended snow cover till May during that year. The amplitude of R_n, LE, H and G were smaller compared to the 2015-16 year.

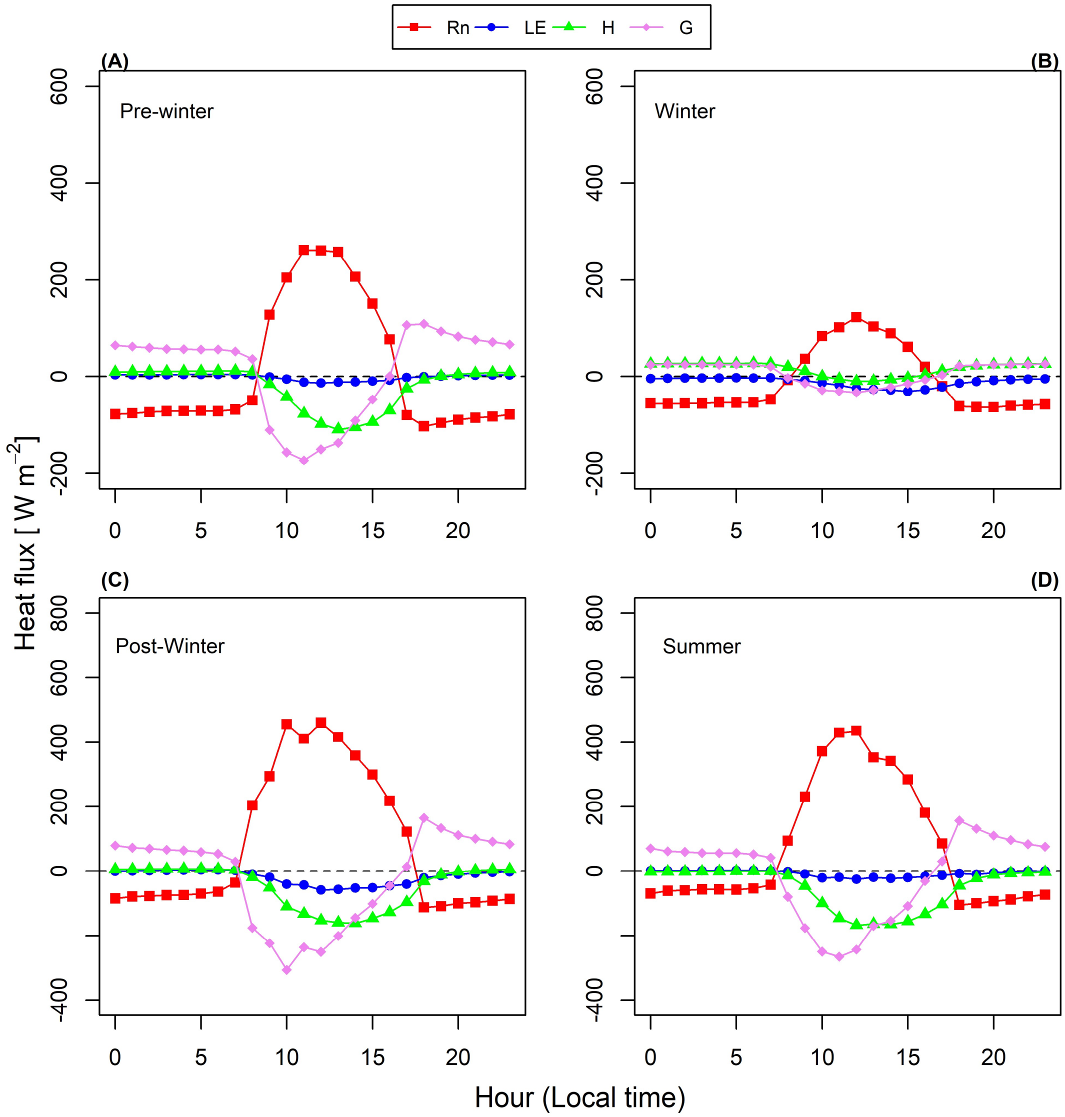

Figure S6: The diurnal change of modelled surface energy fluxes on (A) pre-winter, (B) winter, (C) post-winter, and (D) summer seasons for the 2015-16 year at South-Pullu (4727 m a.s.l.), in the upper Ganglass catchment, Leh.

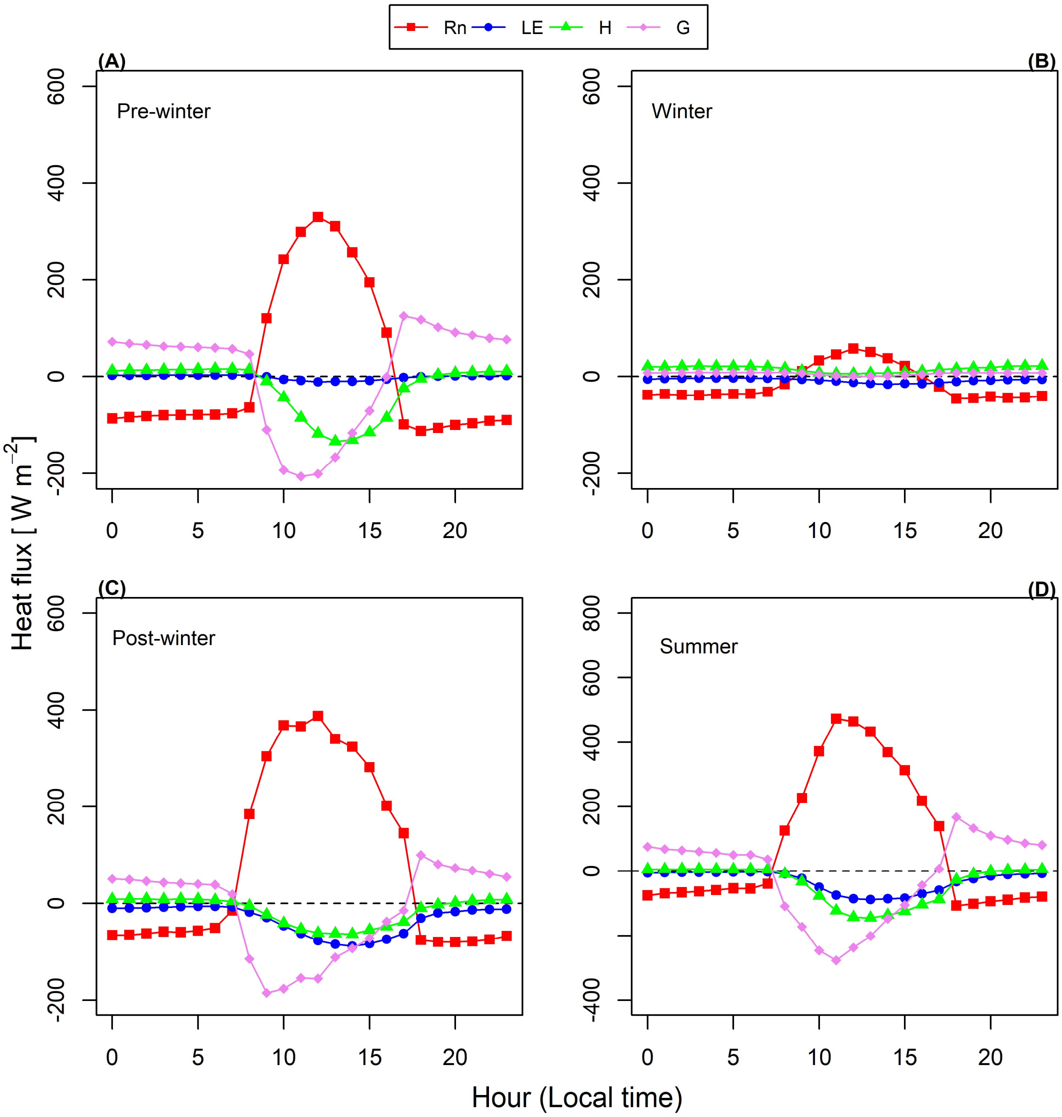

Figure S7: The diurnal change of modelled surface energy fluxes on (A) pre-winter, (B) winter, (C) post-winter, and (D) summer seasons for the 2016-17 year at South-Pullu (4727 m a.s.l.), in the upper Ganglass catchment, Leh.

APPENDICES

APPENDIX-I

Table A1: Snow characterisation parameters used as input to the GEOtop model.

GEOtop parameter name	Description	Units	Value
MaxWaterEqSnowLayerContent	Maximum water equivalent admitted in a snow layer	kg m^{-2}	7
SWEtop	Maximum snow water equivalent per unit area of the snowpack in the top region	kg m^{-2}	3000
SWEbottom	Maximum snow water equivalent per unit area of the snowpack in the bottom region	kg m^{-2}	3000
MaxSnowLayersMiddle	maximum number of layers admitted in middle region	-	50

Table A2: Snow characterisation parameters used as input to the GEOtop model. The parameter values were adopted from Gubler et al. (2013) and Engel et al. (2017).

GEOtop parameter name	Description	Units	Value
SnowCorrFactor	Correction factor on fresh snow accumulation	-	1.8
RainCorrFactor	Correction factor on rain	-	1.0
DewTempOrNormTemp	Use dew temperature (1) or air temperature (0) to discriminate between snowfall and rainfall	-	0
ThresTempRain	Air temperature above which all precipitation is rain	°C	3
ThresTempSnow	Air temperature below which all precipitation is snow	°C	-1
SnowEmissiv	Emissivity of snow	-	0.98
IrriducibleWatSatSnow	Irreducible water saturation. It is the ratio of the capillarity-hold water to ice content in the snow.	-	0.07
MaxSnowPorosity	Maximum snow porosity allowed. This parameter prevents excessive snow densification	-	0.7
DrySnowDefRate	Snow compaction (% per hour) due to destructive metamorphism for snow density < SnowDensityCutoff and dry snow	-	1
SnowDensityCutoff	Snow density cut off to change snow deformation rate	kg m^{-3}	175
WetSnowDefRate	Enhancement factor in presence of wet snow	-	1.5
SnowViscosity	Viscosity of snow	N s m^{-2}	6.E6
AlphaSnow	Freezing characteristic soil for snow	-	1.E5
FreshSnowReflVis	Visible band reflectance of fresh snow	-	0.85
FreshSnowReflNIR	Near infrared band reflectance of fresh snow	-	0.65
AlbExtParSnow	Albedo extinction parameter (aep): if snow depth < aep, albedo is interpolated between soil and snow	mm	10
SnowRoughness	Roughness of snow surface	mm	2
SnowAgingCoeffVis	Reflectance of the new snow in the visible wave length	-	0.2
SnowAgingCoeffNIR	Reflectance of the new snow in the infrared wave length	-	0.5

Table A3: Soil parameters for different groups used as input to the GEOtop model. The parameter values were adopted from Gubler et al. (2013).

GEOtop parameter name	Description	Units	Clay	Silt	Bedrock
AlphaVanGenuchten	Van Genuchten parameter α	m^{-1}	0.001	0.001	0.001
NVanGenuchten	Van Genuchten parameter n	-	1.6	1.4	1.2
ThermalConductivitySoilSolids	Thermal conductivity of the soil solid	$W\ m^{-1}\ K^{-1}$	2.5	2.5	2.5
ThermalCapacitySoilSolids	Thermal capacity of the soil solid	$10^6\ J\ m^{-3}\ K^{-1}$	2.25	2.25	2.25
ThetaSat	Saturated water content	%	0.49	0.47	0.47
ThetaRes	Residual water content	%	0.06	0.07	0.002

Table A4: Soil and ground surface characterisation parameters used as input to the GEOtop model. The parameter values were adopted from Gubler et al. (2013).

GEOtop parameter name	Description	Units	Value
SoilLayerThicknesses	vector defining the thickness of the various soil layers	mm	19 layers with thickness increasing from the surface to the deeper layers
Simulation depth		m	10
InitSoilTemp	Initial soil temperature	°C	-0.5
BottomBoundaryHeatFlux	Incoming heat flux at the bottom boundary of the soil domain (geothermal heat flux)	W m^{-2}	0
SoilRoughness	Roughness length of soil surface	mm	10
ThresSnowSoilRough	Threshold on snow depth to change roughness to snow roughness values with d0 set at 0, for bare soil fraction	mm	2
SoilAlbVisDry	Ground surface albedo without snow in the visible - dry	-	0.20
SoilAlbNIRDry	Ground surface albedo without snow in the near infrared - dry	-	0.20
SoilAlbVisWet	Ground surface albedo without snow in the visible - saturated	-	0.18
SoilAlbNIRWet	Ground surface albedo without snow in the near infrared - saturated	-	0.18
SoilEmissiv	Ground surface emissivity	-	0.88

References

Badescu, V., Gueymard, C. A., Cheval, S., Oprea, C., Baciu, M., Dumitrescu, A., Iacobescu, F., Milos, I. and Rada, C.: Computing global and diffuse solar hourly irradiation on clear sky. Review and testing of 54 models, Renew. Sustain. Energy Rev., 16(3), 1636–1656, doi:10.1016/j.rser.2011.12.010, 2012.

Carslaw, D. C. and Ropkins, K.: openair — An R package for air quality data analysis, Environ. Model. Softw., 27–28, 52–61, doi:10.1016/j.envsoft.2011.09.008, 2012.

Engel, M., Notarnicola, C., Endrizzi, S. and Bertoldi, G.: Snow model sensitivity analysis to understand spatial and temporal snow dynamics in a high-elevation catchment, Hydrol. Process., 31(23), 4151–4168, doi:10.1002/hyp.11314, 2017.

Gubler, S., Gruber, S. and Purves, R. S.: Uncertainties of parameterized surface downward clear-sky shortwave and all-sky longwave radiation., Atmos. Chem. Phys., 12(11), 5077–5098, doi:10.5194/acp-12-5077-2012, 2012.

Gueymard, C. A.: Clear-sky irradiance predictions for solar resource mapping and large-scale applications: Improved validation methodology and detailed performance analysis of 18 broadband radiative models, Sol. Energy, 86(8), 2145–2169, doi:10.1016/j.solener.2011.11.011, 2012.

Moriasi, D. N., Arnold, J. G., Liew, M. W. Van, Bingner, R. L., Harmel, R. D. and Veith, T. L.: Model evaluation guidelines for systematic quantification of accuracy in watershed simulations, Am. Soc. Agric. Biol. Eng., 50(3), 885–900 [online] Available from: https://pubag.nal.usda.gov/catalog/9298, 2007.

Nash, J. E. and Sutcliffe, J. V.: River flow forecasting through conceptual models part I — A discussion of principles, J. Hydrol., 10(3), 282–290, doi:10.1016/0022-1694(70)90255-6, 1970.

Stow, C. A., Roessler, C., Borsuk, M. E., Bowen, J. D. and Reckhow, K. H.: Comparison of Estuarine Water Quality Models for Total Maximum Daily Load Development in Neuse River Estuary, J. Water Resour. Plan. Manag., 129(4), 307–314, doi:10.1061/(ASCE)0733-9496(2003)129:4(307), 2003.